J. Fluid Mech. (1990), *vol.* 210, *pp.* 565–591
Printed in Great Britain

Axisymmetric creeping motion of drops through circular tubes

By M. J. MARTINEZ† AND K. S. UDELL
Department of Mechanical Engineering, University of California at Berkeley, Berkeley, CA 94720, USA

(Received 25 October 1988 and in revised form 28 June 1989)

The axisymmetric creeping motion of a neutrally buoyant deformable drop flowing through a circular tube is analysed with a boundary integral equation method. The fluids are immiscible, incompressible, and the bulk flow rate is constant. The drop to suspending fluid viscosity ratio is arbitrary and the drop radius varies from 0.5 to 1.15 tube radii. The effects of the capillary number, viscosity ratio, and drop size on the deformation, the drop speed, and the additional pressure loss are examined.

Drops with radius ratios less than 0.7 are insensitive to substantial variation in capillary number and viscosity ratio, and computed values of drop speed and extra pressure loss are in excellent agreement with small deformation theories (Hestroni *et al.* 1970; Hyman & Skalak 1972*a*). For this drop size range, significant deformation will result only for $Ca > 0.25$. The onset of a re-entrant cavity is predicted at the trailing end of the drop for $Ca \approx 0.75$. Drop speed and meniscus shape become independent of drop size for radius ratios as small as 1.10. The extra pressure loss can be positive or negative depending mainly on the viscosity ratio, however a relatively inviscid drop can cause a positive extra pressure loss when capillary forces are significant. Computed values for extra pressure loss and drop speed are in good agreement with the experimental data of Ho & Leal (1975) for drops of sizes comparable with the tube radius.

1. Introduction

The motion of deformable drops and bubbles in circular tubes is of interest in a wide range of industrial and technical applications. The flow system arises in many processing flows and is of intrinsic interest to the rheology of suspensions. The flow of bubbles and drops in a circular tube has also been used as a model of the flow of blood cells through the capillaries (Prothero & Burton 1961; Hyman & Skalak 1972*a*, *b*).

This system is also important as a pore model of two-phase flow through porous materials and in particular as a model of the displacement of residual oil from geologic strata during enhanced oil recovery. Early attempts to attach physical significance to the concept of the permeability of a porous material utilized the analogy between Darcy's law and the Hagen–Poiseuille law. This led to the use of the bundle of capillary tubes as a mathematical model for establishing the relation between permeability and porous medium characteristics such as porosity, specific surface area, and tortuosity. Scheidegger (1974), and Dullien (1979) review these and other related models of permeability. More recent models recognize the extensional

† Current address: Fluid and Thermal Sciences Department, Sandia National Laboratories, Albuquerque, NM 87185, USA.

character of the flow along the sinuous paths of a porous material and use varying-area tubes to better model pore geometry (Payatakes, Tien & Turian 1973; Payatakes & Niera 1977; Payatakes 1982; Olbricht & Leal 1983; Martinez 1987). Although a straight or constricted tube is a gross over-simplification of the true pore geometry of geologic material, the effects of bounding walls, non-uniform strain due to constrictions, interfacial tension, drop volume, and viscosity ratio on the pressure gradient to volume flux relation can be examined. This latter function is of interest in the macroscopic Darcy flow description of multiphase fluid transport in porous media.

Theoretical studies of the flow of drops and particles in circular tubes began by considering small particles with little or no deformation. Haberman & Sayre (1958) (see also Happel & Brenner 1965) considered isolated spherical particles and liquid drops in axisymmetric motion in a infinite tube by analytical and numerical means. Hestroni, Haber & Wacholder (1970) treated the case of a small spherical drop or bubble moving axially at an arbitrary radial location within the tube. Their result for a neutrally buoyant drop in axisymmetric motion gives the reduction in drop velocity as quadratic in drop size. They used this approximate solution for an undeformed drop in the normal stress balance on the fluid interface to obtain a leading-order approximation to the deformed drop shape, valid for vanishing capillary number. Brenner (1971) used the solution of Hestroni *et al.* in a reciprocal theorem for creeping flow to obtain the extra pressure decrease due to the presence of the drop suspended in the bulk flow. Brenner's results show that if the drop to suspending fluid viscosity ratio, λ, is 0.48 or less the suspension can flow at the same bulk velocity, V, with less pressure difference than required for the suspending fluid alone.

For small to intermediate drop sizes, Hyman & Skalak (1972*a*, *b*) considered the axisymmetric flow of a train of equally spaced drops in a circular tube as a model of blood flow in the capillaries. They considered both undeformed and deformed drops for arbitrary viscosity ratio and drop spacing. However, owing to lack of convergence in their series solution, they were restricted to drop sizes in the range $a_0/R_0 \leqslant 0.8$ for undeformed drops and to $a_0/R_0 \leqslant 0.7$ for deformed drops, where a_0 is the undeformed drop radius and R_0 is the tube radius. Their results indicate that drop interactions vanish for drop spacing as small as one tube diameter. Chi† (1986) also considered axisymmetric motions of drops, obtaining numerical solutions with a boundary integral method. His work focused on the effects of large capillary number, mainly for $a_0/R_0 = 0.7$, and reports a re-entrant cavity at the trailing end in this parameter range. No evaluations of pressure drop are reported by Chi.

For drops of undeformed diameter comparable with the tube diameter, an experimental investigation of a train of neutrally buoyant drops, spaced so as to eliminate drop interactions, was carried out by Ho & Leal (1975). Their results covered the range $0.726 \leqslant a_0/R_0 \leqslant 1.10$ for λ varying from about 0.2 to 2. They measured the variation of drop velocity, U, and extra pressure decrease, ΔP^+, with the drop size, bulk velocity and viscosity ratio and also carried out a flow visualization of the system in a frame moving with the drops. They confirmed the theoretical predictions that ΔP^+ is negative if λ is small. Direct comparison of the theory with the experiments is not possible, however, since Ho & Leal's smallest dimensionless drop size of 0.726 just exceeds the largest value of 0.70 computed by Hyman & Skalak for deformed drops. The trends indicate good overlap between theory and experiment.

† We are indebted to a reviewer for bringing this work to our attention.

For $a_0/R_0 \gg 1$, experiments have been conducted for bubble flow ($\lambda = 0$) in capillaries by Fairbrother & Stubbs (1935), Prothero & Burton (1961), Taylor (1961), Cox (1962), Goldsmith & Mason (1963) and Schwartz, Princen & Kiss (1986). Bretherton (1961), using lubrication theory, analysed the problem for $\lambda = 0$ and $Ca(= \mu V/\gamma) \to 0$, where μ is the suspending fluid viscosity and γ is the interfacial tension. Bretherton also carried out experiments for comparison to his theory, and found good agreement for $10^{-4} \leqslant \mu U/\gamma \leqslant 5 \times 10^{-3}$. The theory underpredicts the measured values of film thickness for smaller Ca. Teletzke (1983) recently extended Bretherton's analysis to arbitrary values of λ, also for vanishing Ca. For arbitrary Ca and $\lambda = 0$, numerical investigations are required and have been carried out for the leading meniscus of a semi-infinite bubble by Reinelt & Saffman (1985), using finite differences, and by Shen & Udell (1985), using finite elements. Martinez & Udell (1989) consider both the leading and trailing menisci of a long inviscid bubble using a boundary integral equation method. Goldsmith & Mason (1963) carried out experiments both for long drops and bubbles ($\lambda = 0$). These investigations are important as models of displacement in small capillaries and in Hele-Shaw cells. The major focus has been the evaluation of U/V and of the film thickness of suspending fluid between the drop or bubble and the tube wall. The pressure difference across the menisci is also important for displacement and has been computed analytically for vanishing capillary number and numerically for finite values.

In the present investigation we consider the axisymmetric creeping motion of a neutrally buoyant deformable drop through a circular tube of radius R_0. The drop to suspending fluid viscosity ratio is arbitrary. The drop size is also arbitrary but the range of most interest is expected to be for $a = a_0/R_0 = O(1)$; asymptotic behaviour is anticipated for large and small a. The problem is formulated as a boundary integral equation to be solved numerically for the unknown values of traction and velocity on the domain boundaries, including the fluid interface. The drop shape is also unknown *a priori* and the kinematic condition on the interface is used to generate a system of ordinary differential equations for the time variation of the coordinates from an initially specified shape to the desired steady drop profile. Once the steady shape and associated boundary velocities and tractions are determined, the drop deformation, the speed, and the extra pressure decrease in the tube due to the presence of the droplet, can be computed. In addition, the fluid velocity interior and exterior to the drop can be computed at any arbitrary point in the fluid domain. These variables are determined as functions of the dimensionless parameters that appear in the problem, viz. the undeformed drop radius to tube radius ratio, a, the drop to suspending fluid viscosity ratio, λ, and the capillary number, $Ca = \mu V/\gamma$, which measures the relative importance of viscous stresses to surface-tension-induced stresses. If the drop is not neutrally buoyant the Bond number, $Bo = (\rho - \rho_b)\, gR_0^2/\gamma$, is also relevant and measures the buoyancy relative to the surface tension forces. For generality, the problem formulation includes the effects of buoyancy, although only axisymmetric, neutrally buoyant problems are ultimately considered.

The formulation of the fluid interface problem including the appropriate boundary conditions and a scheme, based upon the kinematic condition, to determine the steady shape are discussed. Details of the construction of a boundary integral equation for the axisymmetric, two-fluid problem are presented along with the method of computing the velocity vector in either fluid. The numerical treatment, using various finite element techniques, follows. Results of the analysis are presented for a significant subset of the parameter space, particularly for the range of drop size pertinent to multiphase flows in porous media. The results are compared, where

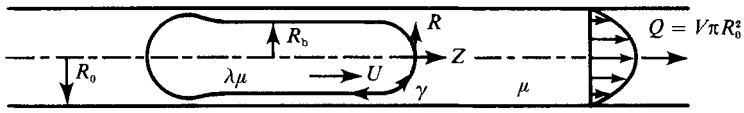

FIGURE 1. Steady translation of a viscous drop in a liquid-filled tube.

appropriate, to existing analytical and experimental investigations. Finally, the major results of the analysis are summarized.

2. Theoretical formulation

Consider the axisymmetric creeping motion of a drop with viscosity $\lambda\mu$ translating steadily with speed U in a tube filled with another liquid of viscosity μ as shown in figure 1. The fluids are immiscible and a constant surface tension, γ, is exerted along their common interface. The volume of the drop is $4\pi(a_0)^3/3$, where a_0 is its undeformed radius. Both fluids are incompressible and the suspending fluid flows at constant discharge, Q, with a steady Poiseuille distribution far ahead and behind the drop. Gravitational body forces can be included, so long as they act along the symmetry axis such that the motion remains axisymmetric.

The velocity, $\boldsymbol{v}$, and pressure, p, of the suspending fluid are governed by continuity and the Stokes approximation for momentum balance,

$$\nabla\cdot\boldsymbol{v} = 0 \quad \text{for} \quad \boldsymbol{x}\in\Omega+\Gamma, \tag{1a}$$

$$\nabla\cdot\boldsymbol{\sigma}(\boldsymbol{v}) = \boldsymbol{0} \quad \text{for} \quad \boldsymbol{x}\in\Omega, \tag{1b}$$

$$\boldsymbol{\sigma}(\boldsymbol{v}) = -p\boldsymbol{I}+\mu[\nabla\boldsymbol{v}+(\nabla\boldsymbol{v})^{\mathrm{T}}], \tag{2}$$

where Ω denotes the suspending fluid domain with boundary Γ, including the tube walls, an inflow and outflow plane, and the fluid interface. The corresponding equations for velocity and pressure in the drop are given by,

$$\nabla\cdot\boldsymbol{u} = 0 \quad \text{for} \quad \boldsymbol{x}\in\Omega_{\mathrm{B}}+\Gamma_{\mathrm{B}}, \tag{3a}$$

$$\nabla\cdot\boldsymbol{\sigma}(\boldsymbol{u}) = \boldsymbol{0} \quad \text{for} \quad \boldsymbol{x}\in\Omega_{\mathrm{B}}, \tag{3b}$$

$$\boldsymbol{\sigma}(\boldsymbol{u}) = -p_{\mathrm{b}}\boldsymbol{I}+\lambda\mu[\nabla\boldsymbol{u}+(\nabla\boldsymbol{u})^{\mathrm{T}}], \tag{4}$$

where Ω_{B} denotes the drop fluid domain and Γ_{B} the interface between the two fluids. In these equations, p and p_{b} are the dynamic pressures,

$$p = P+\rho gZ, \quad p_{\mathrm{b}} = P_{\mathrm{b}}+\rho_{\mathrm{b}}gZ,$$

where P and P_{b} are the total fluid pressures, ρ and ρ_{b} are the fluid densities, and g is the gravitational acceleration acting in the direction of decreasing Z, the coordinate along the axis of symmetry. The dynamic pressure measures the fluid pressure in excess of the hydrostatic contribution and will simply be referred to as the pressure, without special designation, in the remainder of this paper.

In the equations to follow, lengths are non-dimensionalized with the tube radius, R_0, velocity with the bulk velocity, $V(=Q/\pi R_0^2)$, pressure and stress with $\mu V/R_0$, and

time with R_0/V. The boundary conditions written in non-dimensional variables and with respect to a reference frame moving with the drop are

$$\boldsymbol{v} \equiv \boldsymbol{V} = \begin{cases} \left[2(1-r^2)-\dfrac{U}{V}\right]\boldsymbol{e}_z & \text{as} \quad z \to \pm\infty \\ -\dfrac{U}{V}\boldsymbol{e}_z & \text{on} \quad r=1 \end{cases} \tag{5}$$

on the tube and

$$\boldsymbol{v} = \boldsymbol{u} \quad \text{for} \quad \boldsymbol{x} \in \Gamma_B, \tag{6a}$$

$$\boldsymbol{\sigma}(\boldsymbol{v})\cdot\boldsymbol{n} - \boldsymbol{\sigma}(\boldsymbol{u})\cdot\boldsymbol{n} = \frac{1}{Ca}(\kappa - Bo\, z)\boldsymbol{n} \quad \text{for} \quad \boldsymbol{x} \in \Gamma_B, \tag{6b}$$

on the fluid interface. There is also a kinematic condition on the interface requiring that the interface move normal to itself at the local normal velocity,

$$\frac{\partial \boldsymbol{Y}}{\partial t}(\boldsymbol{X}, t)\cdot\boldsymbol{n} = \boldsymbol{v}\cdot\boldsymbol{n}, \tag{7}$$

where $\boldsymbol{Y}(\boldsymbol{X}, t)$ is the position vector of a point on the interface. In these boundary conditions, $\boldsymbol{n}$ is the unit normal to Γ_B directed outward from the suspending fluid, and κ is the interface curvature non-dimensionalized by the tube radius. The boundary conditions on the tube are a fully developed Poiseuille flow far ahead and behind the drop and the no-slip condition on the tube wall. The interface is a material surface on which the velocities are continuous and the stresses are discontinuous in the normal direction by an amount proportional to the interface curvature. The three conditions on the interface do not overspecify the problem since the steady shape is unknown *a priori* and must be determined as part of the solution.

It is convenient to reformulate this fluid interface problem as a boundary integral equation for the unknown velocity on the interface and stress on the tube wall. A reformation as a boundary integral equation enjoys several significant advantages for fluid interface problems in general. One advantage, which is gained for any boundary integral equation representation of a boundary value problem, is the reduction in dimension; the axisymmetric problem can be reduced to a vector line integral along the generating curve in a meridional plane. Furthermore, the method is particularly efficient for the fluid interface problem where the shape is to be determined as part of the solution since the boundary velocities on the interface are determined directly without need of solving for the entire velocity field. The surface velocity, through the kinematic condition, defines the rate of deformation of the fluid interface. Finally, troublesome features associated with dynamic mesh specification, characteristic of domain methods such as finite difference and finite element, are greatly reduced.

The construction of a boundary integral equation for elastostatic analysis of a domain with inclusions of different material properties was discussed by Rizzo & Shippy (1968); the analogous problem of the deformation of a liquid droplet suspended in another liquid was discussed by Rallison & Acrivos (1978) for the exterior problem in Stokes flow. Our development for the interior problem is similar to these earlier discussions. The general scheme is to reformulate the problem for each different fluid as a boundary integral equation relating the stress and velocities on the bounding surface of the considered domain. The boundary conditions on the

fluid interface can be used directly in the reformulation leaving the kinematic condition to determine the steady shape.

Ladyzhenskaya (1969) gives a general solution to the incompressible Stokes equations in an interior domain Ω with boundary Γ. In non-dimensional variables, the solution, applied to the suspending fluid domain, is

$$v_k(\boldsymbol{x}) = \int_\Gamma T_{ik}(\boldsymbol{x},\boldsymbol{y})\, v_i(\boldsymbol{y})\, \mathrm{d}\Gamma(\boldsymbol{y}) - \int_\Gamma U_{ik}(\boldsymbol{x},\boldsymbol{y})\, t_i(\boldsymbol{v}(\boldsymbol{y}))\, \mathrm{d}\Gamma(\boldsymbol{y}), \quad \boldsymbol{x}\in\Omega, \tag{8}$$

where

$$U_{ik}(\boldsymbol{x},\boldsymbol{y}) = -\frac{1}{8\pi}\left[\frac{\delta_{ik}}{|\boldsymbol{x}-\boldsymbol{y}|} + \frac{(x_i-y_i)(x_k-y_k)}{|\boldsymbol{x}-\boldsymbol{y}|^3}\right],$$

$$T_{ik}(\boldsymbol{x},\boldsymbol{y}) = -\frac{3}{4\pi}\frac{(x_i-y_i)(x_j-y_j)(x_k-y_k)}{|\boldsymbol{x}-\boldsymbol{y}|^5} n_j(\boldsymbol{y}).$$

This solution gives the velocity at a field point, $v_k(\boldsymbol{x})$, in terms of the velocities, $v_i(\boldsymbol{y})$, and tractions, $t_i(\boldsymbol{v}(\boldsymbol{y})) = \sigma_{ik}\, n_k$, on the boundary. $\boldsymbol{n}(\boldsymbol{y})$ is the outward pointing normal to the boundary. In a well-posed boundary value problem, either the velocity or traction (or some combination of these) is specified, leaving the other to be determined. The equation (8) can be used to determine this unknown boundary vector if it is converted to a boundary integral equation by letting $\boldsymbol{x}\to\Gamma$ from Ω. The limiting procedure is indicated here because the stress kernel, $\boldsymbol{T}(\boldsymbol{x},\boldsymbol{y})$, suffers a jump as the field point passes from the interior to the boundary (Ladyzhenskaya 1969). The resulting boundary integral equation can be written in a general form as

$$C_{ki}\, v_i(\boldsymbol{x}) + \int_\Gamma T_{ik}(\boldsymbol{x},\boldsymbol{y})\, v_i(\boldsymbol{y})\, \mathrm{d}\Gamma(\boldsymbol{y}) = \int_\Gamma U_{ik}(\boldsymbol{x},\boldsymbol{y})\, t_i(\boldsymbol{v}(\boldsymbol{y}))\, \mathrm{d}\Gamma(\boldsymbol{y}), \quad \boldsymbol{x}\in\Gamma, \tag{9}$$

where $\boldsymbol{C}$ includes the principal value from the jump in the stress kernel, $\boldsymbol{T}$, as $\boldsymbol{x}$ passes from the interior to the boundary. The value of $\boldsymbol{C}$ depends upon the smoothness of the boundary at the point $\boldsymbol{x}$. In particular, $\boldsymbol{C} = -\frac{1}{2}\boldsymbol{I}$ ($\boldsymbol{I}$ is the unit tensor) at a smooth boundary point, defined as a point having a well-defined local tangent plane. In the form (9), the integral equation is formally valid for $\boldsymbol{x}\in\Omega$ by setting $\boldsymbol{C} = -\boldsymbol{I}$. In the axisymmetric case, to be discussed presently, $\boldsymbol{C}$ can be expressed in terms of the turning angle at an edge of an axisymmetric surface.

A similar procedure gives the boundary integral equation for the fluid interface, $\boldsymbol{x}\in\Gamma_\mathrm{B}$,

$$C_{ki}\, u_i(\boldsymbol{x}) - \int_{\Gamma_\mathrm{B}} T_{ik}(\boldsymbol{x},\boldsymbol{y})\, u_i(\boldsymbol{y})\, \mathrm{d}\Gamma(\boldsymbol{y}) = -\frac{1}{\lambda}\int_{\Gamma_\mathrm{B}} U_{ik}(\boldsymbol{x},\boldsymbol{y})\, t_i(\boldsymbol{u}(\boldsymbol{y}))\, \mathrm{d}\Gamma(\boldsymbol{y}), \tag{10}$$

written in terms of the inward-pointing normal to the drop surface. We also note the form taken by (10) when $\boldsymbol{x}\notin(\Omega_\mathrm{B}+\Gamma_\mathrm{B})$,

$$\int_{\Gamma_\mathrm{B}} T_{ik}(\boldsymbol{x},\boldsymbol{y})\, u_i(\boldsymbol{y})\, \mathrm{d}\Gamma(\boldsymbol{y}) = \frac{1}{\lambda}\int_{\Gamma_\mathrm{B}} U_{ik}(\boldsymbol{x},\boldsymbol{y})\, t_i(\boldsymbol{u}(\boldsymbol{y}))\, \mathrm{d}\Gamma(\boldsymbol{y}), \tag{11}$$

which is most easily proven by considering the so-called Green's formula for the Stokes equations (Ladyzhenskaya 1969). This is a general relation for the integral equation representation of the system (3) using hydrodynamic potentials when the point $\boldsymbol{x}$ lies outside the considered domain and its boundary.

We can now construct the boundary integral formulation of the multiple-domain

problem in the following way. On subtracting (11) from (9) and using the boundary conditions (5) and (6) we obtain for $\boldsymbol{x} \in \Gamma_T$ ($\Gamma = \Gamma_T + \Gamma_B$),

$$C_{ki} V_i(\boldsymbol{x}) + \int_{\Gamma_T} T_{ik} V_i \, d\Gamma + (1-\lambda) \int_{\Gamma_B} T_{ik} v_i \, d\Gamma = \int_{\Gamma_T} U_{ik} t_i(\boldsymbol{v}) \, d\Gamma + \frac{1}{Ca} \int_{\Gamma_B} U_{ik} n_i (\kappa - Bo\, z) \, d\Gamma. \quad (12)$$

Similarly, on adding (9) and (10) and using the boundary conditions we obtain for $\boldsymbol{x} \in \Gamma_B$,

$$(1+\lambda) C_{ki} v_i(\boldsymbol{x}) + \int_{\Gamma_T} T_{ik} V_i \, d\Gamma + (1-\lambda) \int_{\Gamma_B} T_{ik} v_i \, d\Gamma = \int_{\Gamma_T} U_{ik} t_i(\boldsymbol{v}) \, d\Gamma + \frac{1}{Ca} \int_{\Gamma_B} U_{ik} n_i (\kappa - Bo\, z) \, d\Gamma. \quad (13)$$

Equations (12) and (13) are boundary integral equations for the unknown tractions on the tube wall and the surface velocity on the fluid interface. They include all the boundary conditions except the kinematic condition which is left to determine the unknown drop shape. Given the shape of the interface, the equations can be solved to yield the remaining unknown boundary values of velocity and stress. The velocity field anywhere in the fluid domain could then be computed using (8) in the suspending fluid and a similar equation for the drop region. These equations cannot be used directly, however, as they individually require the stress distribution on the interface; the boundary integral equations yield only the jump in the normal component across the interface through the boundary condition (6). A similar procedure to that used above to construct the boundary integral equations (12) and (13) can be applied to construct equations for interior velocities which require only the previously determined boundary values. The resulting equation is the same as (12) if we replace the principal value term, $C_{ki} V_i$, with the following:

$$\begin{array}{ll} -v_k(\boldsymbol{x}) & \text{for } \boldsymbol{x} \in \Omega \\ -\lambda u_k(\boldsymbol{x}) & \text{for } \boldsymbol{x} \in \Omega_B. \end{array} \quad (14)$$

When the geometry and boundary conditions are axisymmetric, the boundary integral equation can be reduced to vector line integrals along the generating curve of the boundary (Youngren & Acrivos 1975). If the equations are written in cylindrical coordinates, the azimuthal integrations can be performed analytically. The resulting form of the equations is similar to (9) and reads

$$\begin{bmatrix} C_{zz} & C_{zr} \\ C_{rz} & C_{rr} \end{bmatrix} \begin{pmatrix} v_z \\ v_r \end{pmatrix} + \int_\Gamma \begin{bmatrix} T_{zz} & T_{zr} \\ T_{rz} & T_{rr} \end{bmatrix} \begin{pmatrix} v_z \\ v_r \end{pmatrix} d\Gamma = \int_\Gamma \begin{bmatrix} U_{zz} & U_{zr} \\ U_{rz} & U_{rr} \end{bmatrix} \begin{pmatrix} t_z \\ t_r \end{pmatrix} d\Gamma. \quad (15)$$

Axisymmetric boundary integral equations corresponding to (12) and (13) follow directly from (15). The principal value tensor, $\boldsymbol{C}$, can be written in a general form in the axisymmetric formulation. In particular, it is useful for the numerical analysis to determine $\boldsymbol{C}$ when the point $\boldsymbol{x}$ lies at an edge of the boundary as shown in figure 2. The principal values are determined by excluding the point $\boldsymbol{x}$ from the region with a piece of the torus. By first writing the stress kernels, T_{ij}, in terms of a local polar coordinate system centred at $\boldsymbol{x}$, the principal values are found by taking the limit as

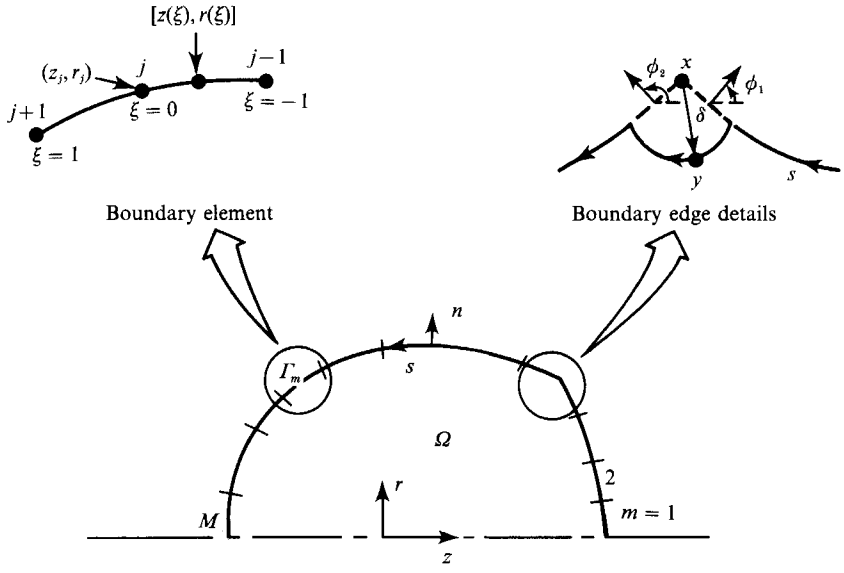

FIGURE 2. Schematic of an axisymmetric boundary and its discretization.

the minor radius of the torus, δ in figure 2, becomes zero. By this procedure the principal value tensor is found to be

$$\boldsymbol{C} = \frac{1}{2\pi}\begin{bmatrix} (\phi_2-\phi_1)-\pi-\frac{1}{2}(\sin 2\phi_2-\sin 2\phi_1) & \frac{1}{2}(\cos 2\phi_2-\cos 2\phi_1) \\ \frac{1}{2}(\cos 2\phi_2-\cos 2\phi_1) & (\phi_2-\phi_1)-\pi+\frac{1}{2}(\sin 2\phi_2-\sin 2\phi_1) \end{bmatrix}.$$

As noted previously, $\boldsymbol{C} = -\frac{1}{2}\boldsymbol{I}$ at a point lying on a smooth portion of the boundary, i.e. when $\phi_2 = \phi_1$. Additional details of this limiting procedure, and of the axisymmetric fundamental solutions, $\boldsymbol{U}$ and $\boldsymbol{T}$, are given in Martinez (1987).

3. Numerical analysis

The numerical solution of the boundary integral equations, (12) and (13), involves the approximation of the integral operators by a linear system to be solved for the unknown stresses and velocities. The boundaries Γ_T and Γ_B are discretized into a total of M boundary elements, each with n_s geometrical boundary nodes. Each curvilinear boundary element is described parametrically according to

$$\begin{pmatrix} z \\ r \end{pmatrix} = \sum_{j=1}^{n_s} \psi_j(\xi)\begin{pmatrix} z_j \\ r_j \end{pmatrix}, \tag{16}$$

where (z_j, r_j) are the cylindrical coordinates of the jth node on the element. The $\psi_j(\xi)$ are Lagrange interpolants defined on the boundary, and the parameter lies in the interval $-1 \leqslant \xi \leqslant 1$, see figure 2. The computer code for this problem was written to allow linear or quadratic variation of the ψ_j with ξ. With this parameterization scheme any axisymmetric boundary geometry can be generally approximated by simply specifying the boundary coordinates corresponding to an appropriate boundary element discretization. A differential element of surface area along the boundary element may be expressed as $\mathrm{d}\Gamma = 2\pi r(\xi)\, J(\xi)\, \mathrm{d}\xi$, where $J(\xi)$ is the Jacobian of transformation,

$$J(\xi) = \frac{\mathrm{d}s}{\mathrm{d}\xi} = [(z_\xi)^2 + (r_\xi)^2]^{\frac{1}{2}},$$

and s is the arclength along the generating curve in a meridional plane. The surface normal and curvature are easily computed in terms of ξ.

The velocity and traction components on each element are also referred to a basis as in the finite element method,

$$\begin{pmatrix} v_z \\ v_r \end{pmatrix} = \sum_{j=1}^{n_b} \phi_j(\xi) \begin{pmatrix} v_{zj} \\ v_{rj} \end{pmatrix}, \tag{17}$$

$$\begin{pmatrix} t_z \\ t_r \end{pmatrix} = \sum_{j=1}^{n_b} \phi_j(\xi) \begin{pmatrix} t_{zj} \\ t_{rj} \end{pmatrix}. \tag{18}$$

Each boundary element contains n_b basis nodes where two unknown components of velocity or traction are to be determined; the total number of basis nodes is N. Note that the basis nodes do not necessarily coincide with the geometrical nodes. Either constant, linear or quadratic basis function, $\boldsymbol{\phi}$ can be specified for $\boldsymbol{v}$ and $\boldsymbol{t}$.

Applying (12) to the basis nodes on Γ_T and (13) to those on Γ_B, and using the approximations presented above, a fully populated $2N \times 2N$ matrix system results and is displayed below to show explicitly the appearance of the parameters,

$$\begin{bmatrix} \boldsymbol{G}^{TT} & \boldsymbol{G}^{TB} \\ \boldsymbol{G}^{BT} & \boldsymbol{G}^{BB} \end{bmatrix} \begin{pmatrix} \boldsymbol{t} \\ \boldsymbol{t}^B \end{pmatrix} = \begin{bmatrix} \boldsymbol{H}^{TT} & (1-\lambda)\boldsymbol{H}^{TB} \\ \boldsymbol{H}^{BT} & (1+\lambda)\boldsymbol{C}^{BB} + (1-\lambda)\hat{\boldsymbol{H}}^{BB} \end{bmatrix} \begin{pmatrix} \boldsymbol{V} \\ \boldsymbol{v} \end{pmatrix}. \tag{19}$$

The matrix $\boldsymbol{G}$ includes numerical coefficients resulting from the inner product of the velocity kernels and basis functions, and $\boldsymbol{H}$ includes those from the traction kernels and basis functions. The submatrix $\boldsymbol{G}^{TB}$, for example, contains the coefficients derived from numerical integration of the boundary integral equation, applied to a boundary point on Γ_T, over a boundary element on Γ_B. $\boldsymbol{C}^{BB}$ is the tri-diagonal submatrix containing the principal values at the basis nodes on the interface and $\boldsymbol{t}^B$ is the vector containing the normal jump in the stress across the interface, e.g.

$$\boldsymbol{t}_j^B = \frac{1}{Ca}(\kappa - Bo\, z)\,\boldsymbol{n}_j$$

for the jth global basis node. The entries in $\boldsymbol{G}$ are calculated according to

$$\begin{bmatrix} G_{2i-1,2j-1} & G_{2i-1,2j} \\ G_{2i,2j-1} & G_{2i,2j} \end{bmatrix} = \int_{-1}^{1} \begin{bmatrix} U_{zz}(\boldsymbol{x}_i, \boldsymbol{y}(\xi)) & U_{zr}(\boldsymbol{x}_i, \boldsymbol{y}(\xi)) \\ U_{rz}(\boldsymbol{x}_i, \boldsymbol{y}(\xi)) & U_{rr}(\boldsymbol{x}_i, \boldsymbol{y}(\xi)) \end{bmatrix} \phi_j(\xi)\, 2\pi r(\xi)\, J(\xi)\, \mathrm{d}\xi$$

which are the element contributions from the basis nodes i and j. Nodes that reside on two contiguous boundary elements contribute two such parts which are summed and assembled into the global matrix (19). A similar equation gives the entries in $\boldsymbol{H}$; these coefficients also include the contribution from $\boldsymbol{C}$. The quadratures are performed numerically over elements Γ_m when $\boldsymbol{x}_i \notin \Gamma_m$. The kernels are improper on elements where $\boldsymbol{x}_i$ is included and the integration is performed on these elements by extracting the singular part, integrating it analytically and summing with the numerical integral of the remainder.

Upon rearranging (19), the linear system,

$$\boldsymbol{A}\boldsymbol{x} = \boldsymbol{f} \tag{20}$$

results where $\boldsymbol{x}$ contains the unknown tractions on the tube and the unknown velocities on the interface,

$$\boldsymbol{x} = \begin{pmatrix} \boldsymbol{t} \\ \boldsymbol{v} \end{pmatrix} = \boldsymbol{A}^{-1}\boldsymbol{f}. \tag{21}$$

The system (20) contains all the boundary conditions except for the kinematic condition which is left to determine the steady shape of the drop. For any given drop shape, the system (20) can be solved for the corresponding velocities on the interface. These can then be used in the kinematic condition to determine the rate of deformation of the interface. The desired shape is the one that yields $\boldsymbol{v}\cdot\boldsymbol{n} = 0$. In the present scheme, the entire problem is solved by specifying an initial estimate of the shape and solving the initial value problem generated by substituting the interface velocities from (21) into the kinematic condition (7). The initial value problem is integrated in time until the steady state is achieved, yielding the desired drop shape.

The time integration was performed using a forward Euler formula in conjunction with a comparison backward Euler step for estimating the local truncation error. The algorithm automatically selects the step sizes such that a local truncation error tolerance is maintained at each step. The steady state was defined as $\|\boldsymbol{v}\cdot\boldsymbol{n}\| < 0.01$ for the velocity vector at node points at the interface. The number of steps required to reach the steady shape varied from about 20 to 100, depending on the initial shape and the parameter set for the problem. The nominal adjustment time to reach the steady solution was about 2 to 4 units of Vt/R_0, or about the time to travel one or two tube diameters. The converged shape from a previously computed problem was used as the initial drop shape for a new problem with a similar parameter set.

The convergence behaviour of this scheme was discussed previously in Martinez & Udell (1989) where it was applied to a similar problem. Briefly, the normal velocity, measured in terms of a norm of the vector of normal velocities on Γ_B, is found to decrease exponentially in time, with time constant as noted above. The only defect of the scheme is that the ordinary differential equations (ODE's) for the history of the coordinates on the fluid interface become stiff for $Ca \ll 1$, owing to large variation in the time constants among the component equations. Time constants for ODE's corresponding to the thin film of suspending fluid between the drop and tube wall, found in small-Ca problems, are much longer than those corresponding to the leading or trailing meniscus. The explicit scheme used here to integrate the ODE's responds to stiffness by reducing the time step, requiring an increasing number of steps to reach the convergence criteria for steady state. However, stiffness is much less of a problem for small Ca in this application than for analysis of long bubbles (Martinez & Udell) where the thin film region is a large fraction of total interfacial area.

The mesh extent on the tube was at least one tube diameter ahead and behind the drop; longer meshes produced no discernible change in results. Between 40 and 80 node points were used on the entire boundary, depending on the drop size considered. Selective comparison with solutions generated with about a 50% increase in the number of nodes resulted in less than 1% difference in results. To maintain a proper discretization, an occasional mesh redistribution was performed by fitting a cubic spline to the polar coordinate representation of the interface. If necessary, the shape was adjusted to maintain the drop volume to within 1% of the specified value. The node spacing was then prescribed according to the local surface curvature, with closer spacing in the regions of largest curvature, and the new initial value problem restarted until another remesh was called for or the steady state was achieved. Computations were performed in single precision on a 32 bit digital machine; comparison of selected single-precision solutions with a double-precision version of the code indicated four significant figures of the precision in the former. Additional details of the numerical analysis are given in Martinez (1987).

4. Discussion of results

In this section the results of the numerical simulations in terms of the effects of the non-dimensional parameters on the flow fields, drop profiles, drop deformation, relative drop speed, and the additional pressure loss are discussed. The discussion begins by first considering the general flow behaviour of the two-phase system as a way of introducing some of the relevant physical mechanisms that are encountered in subsequent discussions. The effects of variation in each non-dimensional parameter on the drop shape, deformation, drop speed, and pressure loss are considered separately. The objective is a logical presentation of results by focusing on one effect at a time, simultaneously offering some insight into the underlying physical mechanism. Many mechanisms are intimately related, however, and it is not always possible to strictly follow this format.

The particular range of parameter values examined in the simulations were chosen both to illustrate their effects over a substantial part of the parameter space and to allow comparison of the present results to available theoretical and experimental results (Hyman & Skalak 1972*a*, *b*; and Ho & Leal 1975). Thus drops with undeformed radii in the interval, $0.5 \leqslant a \leqslant 1.15$ were considered for values of Ca equal to 0.075, 0.1, and 0.15, and for λ equal 0.19, 1.0, 2.04, and 10.0. This drop size range unifies existing theoretical and experimental investigations and permits the demarcation at the lower end where the effect of walls becomes important and at the upper end where the results asymptote to those corresponding to infinitely long drops and bubbles. The values of λ and Ca also coincide with values used by the aforementioned investigators thereby allowing direct comparison to the present results. Furthermore, a study of the effect of viscosity ratio for $0.1 \leqslant \lambda \leqslant 50$ and of the capillary number for $0.05 \leqslant Ca \leqslant 1.0$ is also included for $a = 0.726$.

4.1. *Flow fields*

It is instructive to begin the discussion by illustrating the general flow pattern that results when a neutrally buoyant drop translates steadily in Poiseuille flow. Figure 3 shows the relative velocity vector field in and about a small viscous drop ($a = 0.726$, $\lambda = 10$) and a large, relatively inviscid drop ($a = 1.10$, $\lambda = 0.19$); $Ca = 0.1$ in both cases. Both flow fields are shown in a reference frame that translates with the drop speed; thus the walls move backwards relative to the stationary drop. In this frame, it is apparent that the shear transmitted across the interface results in a recirculation with zero net flux inside the drop. The flow towards the rear, in the interior of the drop, occurs in a shell near the interface whereas the compensating forward flow occurs in the central portion of the drop. An annulus of suspending fluid contiguous with the tube wall moves backwards with respect to the drop.

There are two stagnation rings on the interface reflecting the fact that fluid elements on the tube centreline in the suspending fluid exceed the drop speed while those closer to the tube wall lag behind the drop. The stagnation rings indicate that there is a dividing streamtube separating the net backflow of suspending fluid from a bolus of fluid trapped between each pair of a train of drops. The bolus moves with a bulk speed equal to that of the drops. This interpretation for a train of drops is valid for drop spacings greater than about one tube diameter, according to the analysis of Hyman & Skalak (1972*a*). For an isolated drop, the fluid within the streamtube is being displaced by the drop, while the remaining fluid outside the streamtube is the leak-back flux by-passed by the drop. These flow patterns will likely bear upon the stress distribution on the fluid interface in the presence of

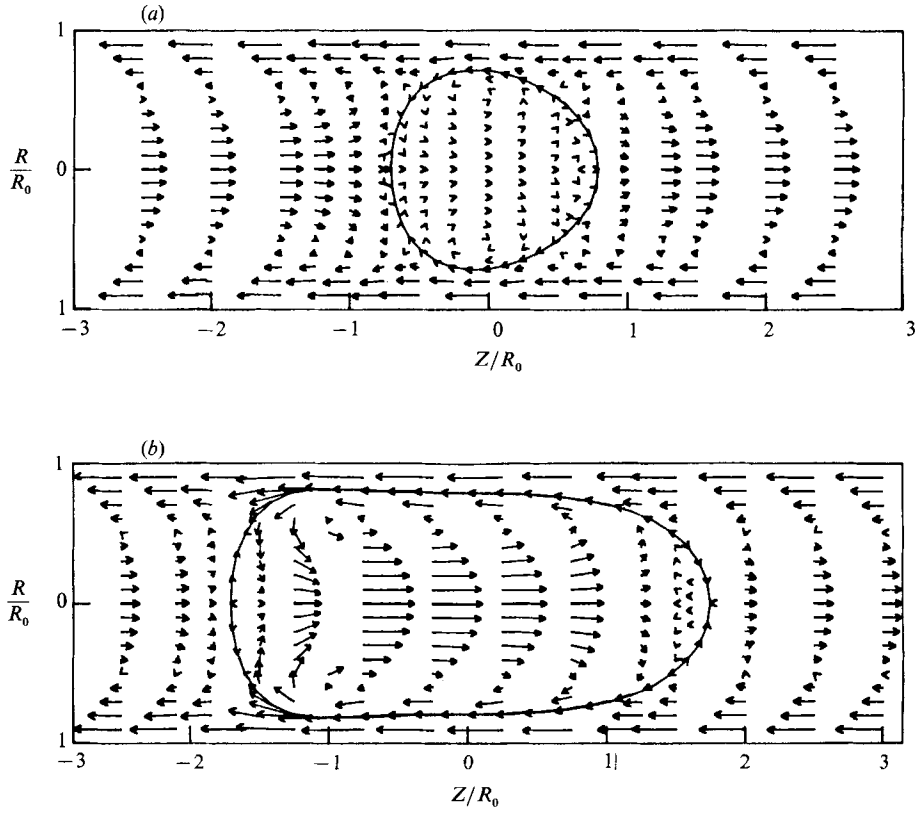

FIGURE 3. Velocity vector field in and about a neutrally buoyant drop suspended in Poiseuille flow: (*a*) $a = 0.726$, $Ca = 0.10$, $\lambda = 10$; (*b*) $a = 1.10$, $Ca = 0.10$, $\lambda = 0.19$.

adsorbed surfactants or impurities, a common situation in flows involving a large amount of interfacial surface area. Convection of surfactant in the vicinity of the stagnation rings may result in a variable surface mobility and can even lead to immobile regions in the case of insoluble surfactants (Davis & Acrivos 1966). These flow patterns are in agreement with previous theoretical and experimental studies of the axisymmetric motion of drops and particles in Poiseuille flow (Taylor 1961; Goldsmith & Mason 1963; Wang & Skalak 1969; and Ho & Leal 1975).

4.2. *Effect of the drop volume*

The variations in drop shape with drop size are shown in figure 4 on which a varies between 0.726 and 1.10. The figure also illustrates the variation in shape with λ. For comparison purposes, the profiles are presented such that the nose of each drop begins at the same spatial location.

The shapes all show a higher curvature at the nose of the drop than at the trailing end. This characteristic profile is in agreement with previous theoretical and experiment investigations (Goldsmith & Mason 1963; Hyman & Skalak 1972*b*, Ho & Leal 1975) and is attributable to several mechanisms particular to Poiseuille flow. In tube flow, sizeable drops are constrained by the tube walls and there is a pressure loss in the direction of flow resulting in higher suspending fluid pressure at the rear of the drop than about the leading end. Since referring axes to a uniformly translating frame leaves the stress distribution unchanged, the flow field responsible

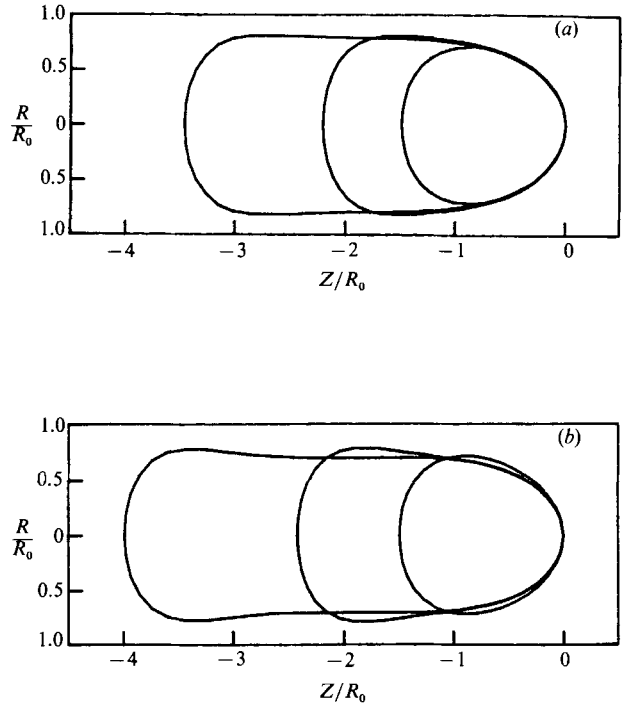

FIGURE 4. Variation in drop shape with drop volume and viscosity ratio for $Ca = 0.10$; $a = 1.10$, 0.914, 0.726 from left to right; (*a*) $\lambda = 0.19$; (*b*) $\lambda = 10$.

for drop deformation can be viewed as that shown in figure 3, which is asymmetric with respect to the drop.

The profiles for drops as large as $a = 0.7$ are only moderately deformed from a spherical shape, even for significant variations in capillary number and viscosity ratio. However, beginning with $a \approx 0.9$, the profiles become appreciably extended for all capillary numbers and viscosity ratios as a result of conforming to the constraint of the tube walls. At the upper end of the size range the computations show that incremental increases in drop volume result in an increase in the length of drop, while the radial extent approaches an asymptotic value. Goldsmith & Mason (1963) report that a film of suspending fluid of constant thickness develops between the front and rear of a steadily translating drop when $a \gg 1$. This asymptotic behaviour in film thickness is noted in the calculations for a slightly greater than one and is further indicated by the approach of the drop radius to a constant value in the central portions of the drop, accompanied by an asymptote to a constant drop speed. The development of an asymptotic film thickness with increasing a is illustrated in figure 5 as it shows that the profiles are unchanging with a except for a lengthening in the axial direction to accommodate the additional volume. The asymptotic shape is nominally attained for $a \approx 1.1$. The thickness of the film of suspending fluid surrounding the drop is, for these cases, dependent only upon the capillary number and viscosity ratio. The computed values are compared with available theoretical and experimental results for long drops and bubbles in figure 6 showing the film thickness variation with capillary number and viscosity ratio. Evidently the film thickens with increasing capillary number owing to the attendant increase in deformation. The film also thickens with increasing viscosity ratio for the same

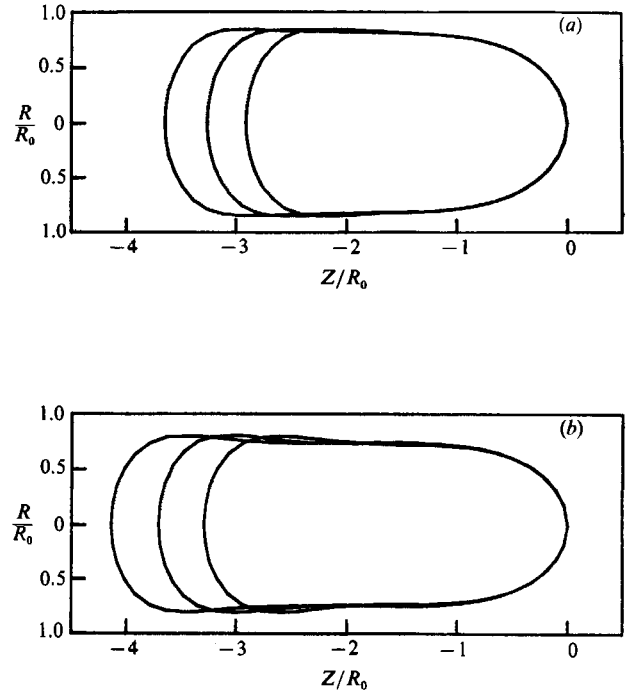

FIGURE 5. Development of an asymptotic film thickness of suspending fluid surrounding the drop for $Ca = 0.10$; $a = 1.15$, 1.10, 1.05 from left to right; (*a*) $\lambda = 0.19$; (*b*) $\lambda = 10$.

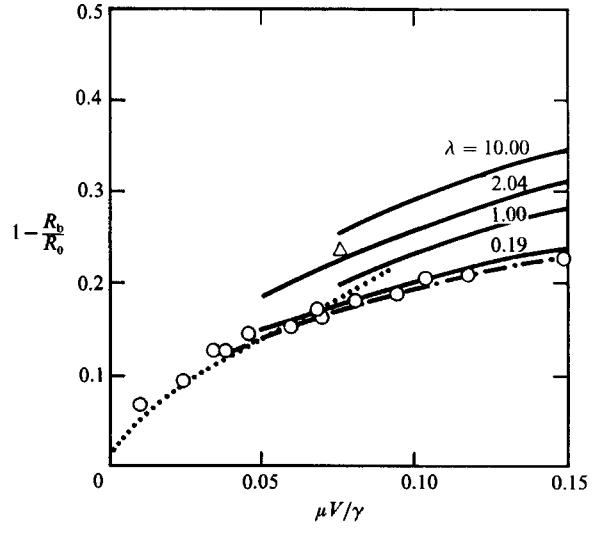

FIGURE 6. Film thickness of suspending fluid as a function of capillary number; ——, present results; —·—, results from Martinez & Udell (1989) for $\lambda = 0$ and $a \to \infty$; ..., Fairbrother & Stubbs (1935); ○, Taylor (1961); △, Goldsmith & Mason (1963), $\lambda = 6$.

capillary number. Increasing viscosity ratio also increases drop deformation since a viscosity contrast across the interface enhances the deforming viscous stresses in the suspending fluid. The film thickness for $\lambda = 0.19$ compares well with the values for $\lambda = 0$ computed by Martinez & Udell (1989) for the leading meniscus of an infinitely long bubble. These numerical results for small λ compare well with the data collected

by Taylor (1961), while the empirical correlation of Fairbrother & Stubbs (1935) is seen to deviate for $Ca > 0.06$. The comparison of the present results to the film thickness for a long drop with $\lambda = 6$ and $Ca = 0.075$, reported by Goldsmith & Mason, is satisfactory.

In the case $a \to \infty$, the leading meniscus is important as a model of the displacement of suspending fluid originally in place by the steady translation of a viscous finger. In this regard it is important to note that although the film of suspending fluid left on the tube wall thickens with increasing viscosity ratio, the leak-back flux is less than for displacement by an inviscid bubble. The inviscid bubble can exert no tangential stresses on the suspending fluid and so leaves the entire film on the wall, while the viscous drop drags film fluid along with it. A more viscous drop leaves less suspending fluid behind if the relative volume flux of the drop decreases with increasing λ for fixed capillary number, i.e.

$$\left(\frac{R_{b(\lambda)}}{R_0}\right)^2 \frac{U_{(\lambda)}}{V} < \left(\frac{R_b}{R_0}\right)^2 \frac{U}{V},$$

where R_b is the asymptotic drop radius and the subscript λ denotes variables corresponding to a more viscous drop than the unsubscripted variables. The inequality is borne out in the calculations as indicated in figures 5, 6, and 13, which show that a more viscous drop has a slower relative drop speed and is surrounded by a thicker film of suspending fluid than a less viscous drop. This observation was also made by Teletzke (1983) who extended the asymptotic analysis of Bretherton (1961) (for $a \to \infty$, $\lambda = 0$, $Ca \to 0$) to arbitrary λ.

In considering the current problem as a model of two-phase flow in a porous structure, the ratio of drop velocity to average bulk velocity is important as a measure of the mobility of the dispersed phase. The speed ratio, U/V, is shown in figure 7 as a function of a for various values of Ca and λ. Also shown are the numerical results of Hyman & Skalak (1972*a*) for undeformed liquid spheres, presumably the limit in shape when $Ca \to 0$, and the experimental data of Ho & Leal (1975) for $0.726 \leqslant a \leqslant 1.10$. The results of Hyman & Skalak show that $U/V \to 2$ at vanishingly small a; thus small drops move at nearly the local suspending fluid speed on the tube centreline. The speed ratio decreases with increasing size, owing to the retarding effect of the no-slip condition, and eventually attains a constant value for $a > 1$ as discussed above. Excellent agreement is found between the results for undeformed drops and the present calculations up to $a \approx 0.7$, above which the effects of size and capillary number on deformation become significant; the deviation in figure 7(*a*) is due to the difference in the values of drop viscosity. The computed velocities exceed the experimental values reported by Ho & Leal by 2–7% over the range of comparable drop sizes. Furthermore, the experimental values show U/V to be a monotonically decreasing function of a until a constant value is attained. The computations, on the other hand, show a minimum in U/V in the range $0.8 \leqslant a \leqslant 1$ when $\lambda \geqslant 1$. Inspection of the numerical solutions shows this minimum to coincide with a maximum in girth in this size range. Thus, according to the computations, a relatively viscous drop of size $a \approx 0.9$ is less easily deformed, has a slightly broader profile, and so moves slightly slower than a larger drop with identical λ and Ca.

The pressure drop required to drive the suspension at the average velocity, V, is of special interest, particularly with regard to the present system as a model of the pore-scale two-phase flow in porous media. A similar relationship between average pressure gradient and velocity in macroscopic flow in porous media involves a proportionality parameter known as the permeability. In the extension of the

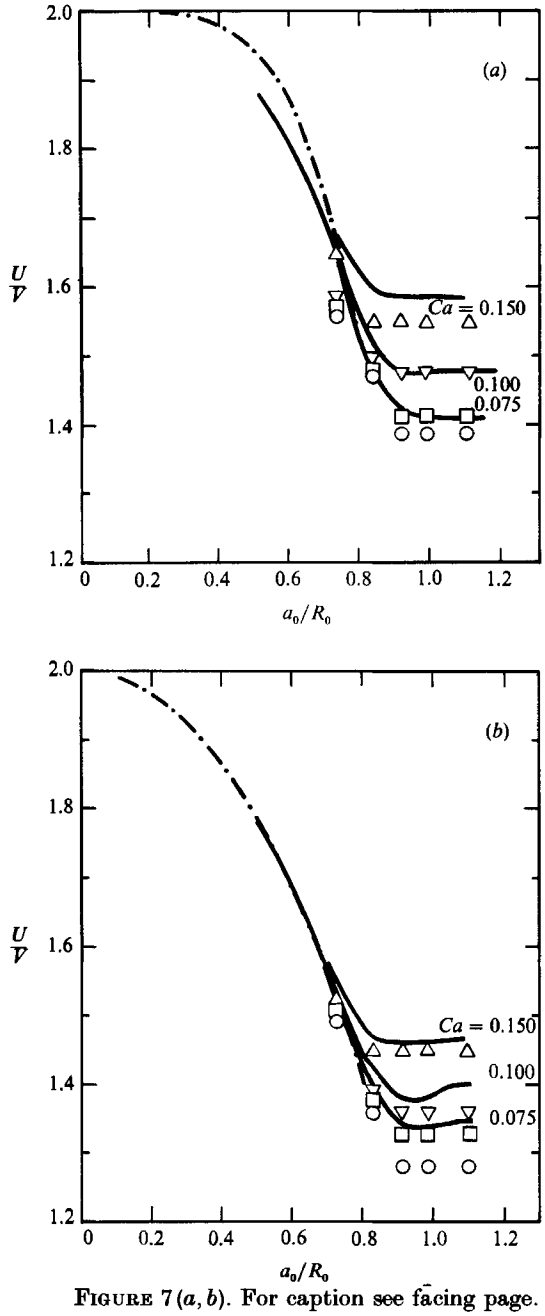

FIGURE 7(a, b). For caption see facing page.

original theory of Darcy (1856) for single-phase flow to multiphase flow, the permeability is assumed to depend mainly on the relative volume fraction of the considered phase (see Scheidegger 1974). The strong effect of drop volume is also seen in the present model problem.

The variation in the extra pressure decrease, ΔP^+, with drop volume is shown in figure 8 for various values of Ca and λ. The results of Hyman & Skalak and of Ho & Leal are also shown for comparison. The extra pressure decrease is defined as the

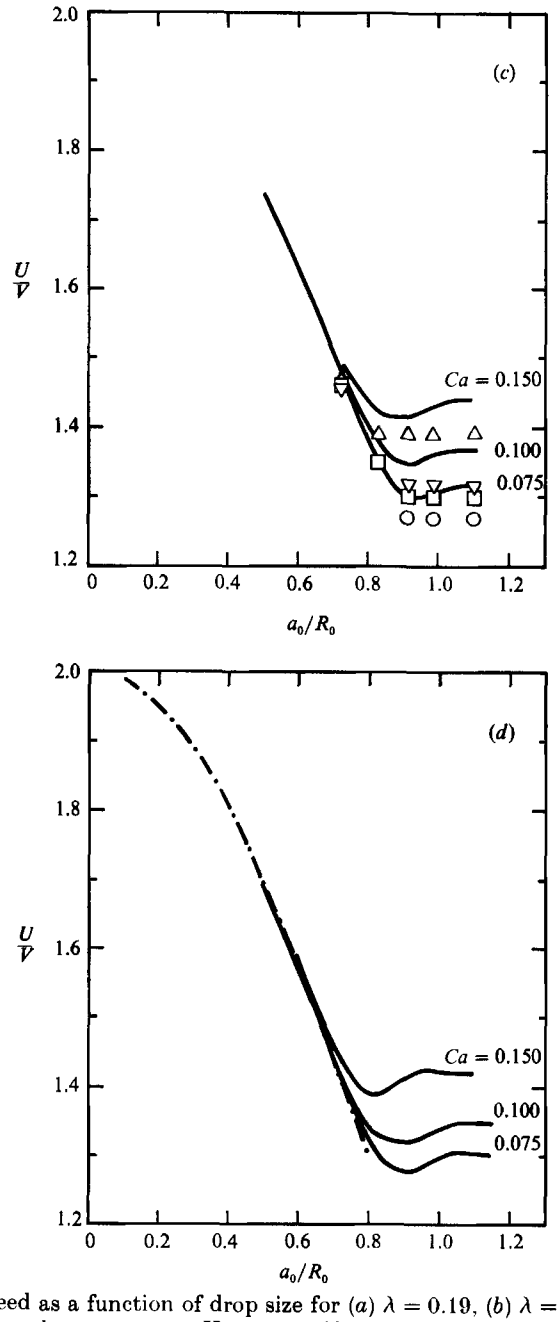

FIGURE 7. Drop speed as a function of drop size for (*a*) $\lambda = 0.19$, (*b*) $\lambda = 1.0$, (*c*) $\lambda = 2.04$, (*d*) $\lambda = 10$: ——, present results; —·—·—, Hyman & Skalak (1972*a*) for undeformed drops and (*a*) $\lambda = 0$. Symbols in (*a*–*c*) are the data of Ho & Leal (1975): ○, $Ca = 0.075$; □, $Ca = 0.100$; ▽, $Ca = 0.150$; △, $Ca = 0.180$.

total pressure decrease over a distance extending into the undisturbed flow ahead of and behind the drop, less the Poiseuille value over the same distance and for the same volume flux of suspending fluid alone. The extra pressure drop represents the local pressure loss due solely to the presence of the drop.

The additional pressure gradient is small when $a < 0.5$; however, ΔP^+ increases (or

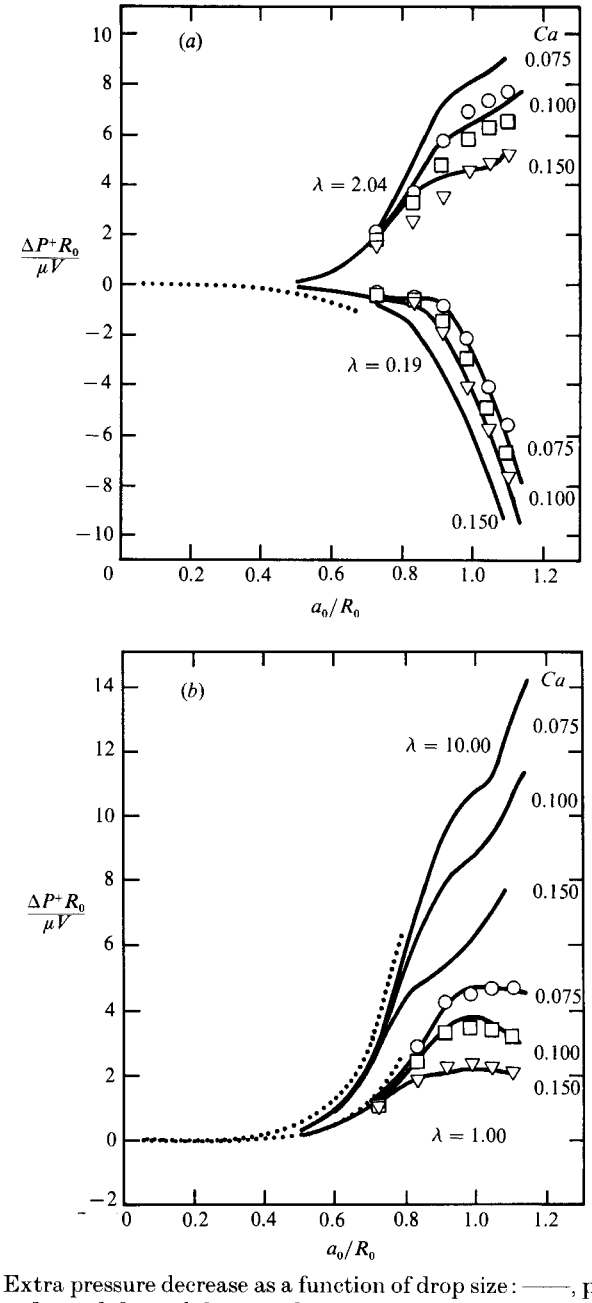

FIGURE 8 (a, b). Extra pressure decrease as a function of drop size: ——, present results; ..., Hyman & Skalak (1972a) for undeformed drops and (a) $\lambda = 0$. Symbols are the data of Ho & Leal (1975): ○, $Ca = 0.075$; □, $Ca = 0.100$; ▽, $Ca = 0.150$.

decreases) dramatically with a thereafter. As we found for U/V, the effects of Ca are significant only for $a > 0.7$. Unfortunately, the effect of drop volume on the extra pressure decrease cannot be fully isolated from effects of viscosity and capillary number when the drop radius is comparable with the tube radius. The viscosity ratio is central to determining whether more or less pressure gradient than the Poiseuille value is required to drive the bulk flow at the same flow rate. Generally, relatively

Ca	λ	r_b	$\frac{\delta\Delta P^+}{\delta a}\frac{R_0}{\mu V}$	$\frac{\partial}{\partial a}\left(\frac{\Delta P^+ R_0}{\mu V}\right)$
0.075	0.19	0.822	−41.6	−39.6
0.10	0.19	0.799	−37.4	−40.3
0.075	10.0	0.745	25.8	28.0
0.10	10.0	0.706	21.6	23.4

TABLE 1. Asymptotic estimation of ΔP^+ for long drops ($a = 1.125$).

inviscid drops result in $\Delta P^+ < 0$ while viscous drops give $\Delta P^+ > 0$, see figure 8. This fluid exchange mechanism will depend strongly on drop volume ($O(a^3)$). In this size range, the capillary number is also important in establishing the sign of ΔP^+ due to wall effects. Strong capillary forces ($Ca \ll 1$) correspond to significant resistance to the deformation required by the lateral constraint of the walls resulting in extra dissipation in satisfying the normal stress jump across the interface. Both the fluid exchange mechanism and the wall effect are included in the analysis of Brenner (1971) showing $\Delta P^+ = O(a^5)$ for moderately small a; the present results show that this strong dependence continues for $a \approx O(1)$, and is more pronounced with extremes in viscosity ratio, i.e. $\lambda \to 0$ and $\lambda \gg 1$.

Asymptotic behaviour as the drop size increases past unity is also observed for ΔP^+ as it was for the shape and speed ratio. In fact, as observed by Ho & Leal (1975), the increase in ΔP^+ with a can be predicted satisfactorily by considering any increase in drop volume to result solely in an increase in length. The corresponding additional pressure loss is estimated by considering as a limiting case two coflowing fluids in tube flow, one of which flows in an annulus adjacent to the tube wall. The pressure gradient is given by (cf. Ho & Leal 1975)

$$\frac{R_0}{\mu V}\frac{\partial(\Delta P^+)}{\partial a} = -32\left(\frac{a}{r_b}\right)^2 \frac{r_b^4}{\frac{\lambda}{1-\lambda}+r_b^4},$$

where r_b is the asymptotic drop radius non-dimensionalized by the tube radius. Computed values in finite difference form, $\delta\Delta P^+/\delta a$, are compared to the above expression in table 1. Thus, at large drop size any increase in pressure loss with drop volume is due mainly to the replacement of the drop volume with fluid of different viscosity.

The comparison of the present results with those of Hyman & Skalak for undeformed drops is excellent for $a \leqslant 0.7$, above which drop deformation is important. The comparison between the data of Ho & Leal and these results for $\lambda \leqslant 1$ is also excellent over the entire overlap range in a (the comparison for $\lambda = 0.58$ is shown in figure 14). The degree of agreement for $\lambda = 0.19$ is, however, capillary-number dependent. The theoretical values of ΔP^+ for $\lambda = 2.04$ are systematically higher than the values reported by Ho & Leal.

4.3. *Effect of the capillary number*

Given the interpretation of the capillary number as a measure of the relative importance of viscous forces to surface-tension-induced forces, its significance in determining the drop shape should come as no surprise. Indeed, besides the more

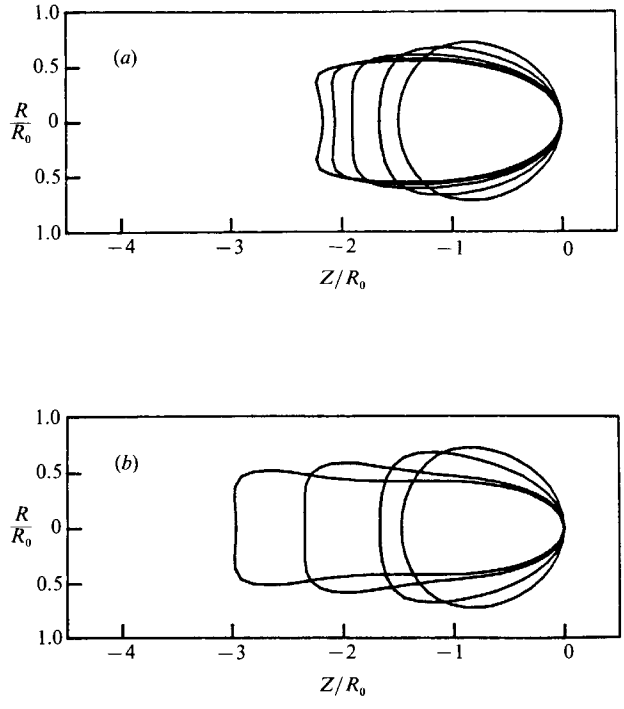

FIGURE 9. Effect of capillary number on drop shape for $a = 0.726$; (*a*) $\lambda = 0.19$ and $Ca = 1.0$, 0.75, 0.50, 0.25, 0.10 from left to right; (*b*) $\lambda = 2.04$ and $Ca = 0.75$, 050, 0.25, 0.10 from left to right.

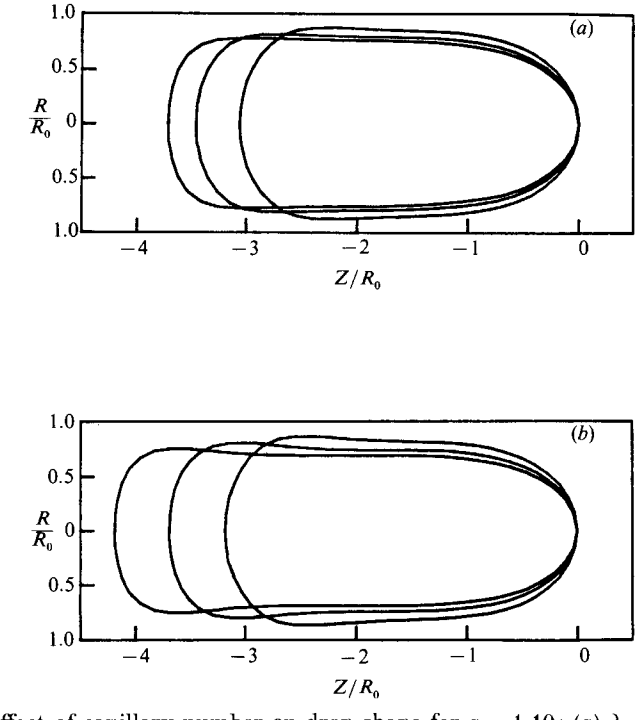

FIGURE 10. Effect of capillary number on drop shape for $a = 1.10$; (*a*) $\lambda = 0.19$ and $Ca = 0.15$, 0.10, 0.05 from left to right; (*b*) $\lambda = 2.04$ and $Ca = 0.15$, 0.10, 0.05 from left to right.

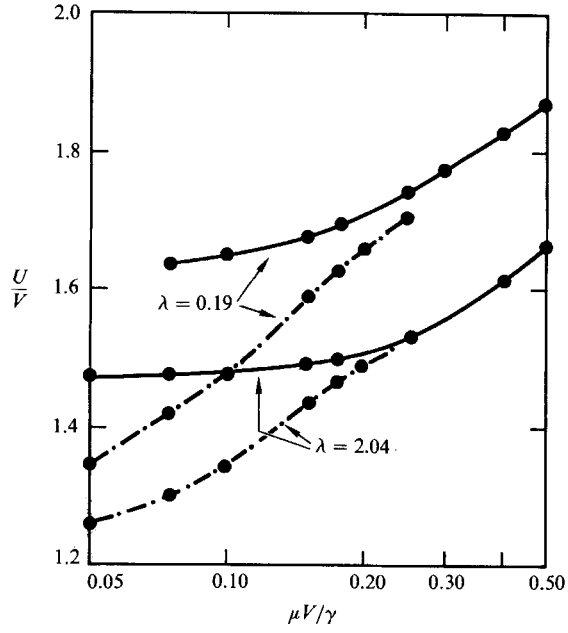

FIGURE 11. Effect of capillary number on drop speed, solid symbols are numerical results: ——, $a = 0.726$; —·—, $a = 0.914$.

obvious effects of drop volume on the deformation (due to constraining walls) the capillary number correlates most readily with the drop deformation. The strong effect of the capillary number on the drop deformation is demonstrated in figure 9 for $a = 0.726$ and in figure 10 for $a = 1.10$, and for a ten-fold increase in λ. The effect of the capillary number on the drop shape is striking, particularly for the small drops where the variation in capillary number is greatest. In all cases, the drop is extended in the direction of flow with increasing Ca. Moreover, the curvature at the leading end increases, while the curvature at the trailing end decreases, with increasing capillary number.

The small drops ($a = 0.726$) develop negative curvature at the rear of the drop beginning with $Ca \approx 0.75$ for both $\lambda = 0.19$ and $\lambda = 2.04$. The same behaviour at large capillary number was noted by Chi (1986) for small a, and by Martinez & Udell (1989) for long inviscid bubbles. Goldsmith & Mason (1963) reported the development of a re-entrant cavity at the rear of long drops and bubbles suspended in a Poiseuille flow at large capillary number. Goldsmith & Mason further observed that at sufficiently high capillary number the suspending fluid penetrated far into the body of the drop in the form of a long thread. The thread broke into a series of smaller drops upon stress relaxation or if the thread penetrated the entire length of the drop. While the present computational scheme cannot explore as large a range in capillary number as that investigated experimentally by Goldsmith & Mason, the results indicate similar behaviour at large capillary number and predict the onset of a re-entrant cavity for $Ca \approx 0.75$.

The effect of the capillary number on the speed ratio, U/V, and the extra pressure decrease, ΔP^+ is shown in figures 11 and 12, respectively (see also figures 7 and 8). In general, the figures show that $\partial(U/V)/\partial Ca > 0$ and $\partial \Delta P^+/\partial Ca < 0$, although the values are strongly dependent on drop size. The relative drop speed for $a = 0.91$ in figure 11, for example, begins substantially lower than that for $a = 0.726$ but

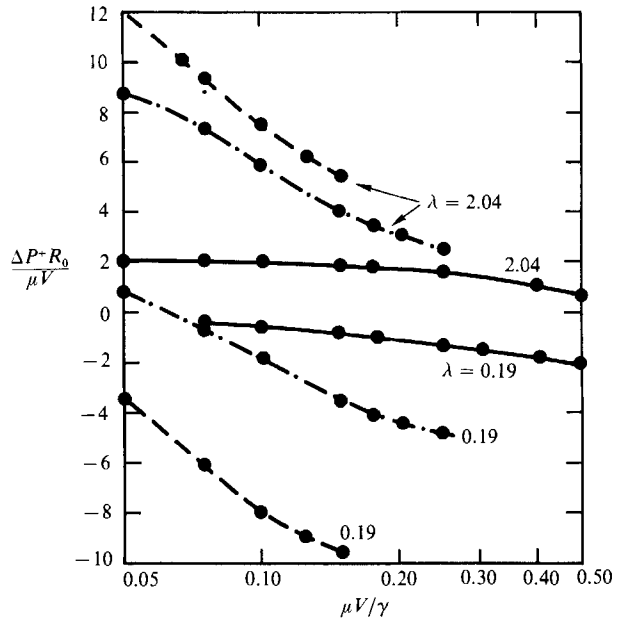

FIGURE 12. Effect of capillary number on extra pressure decrease, solid symbols are numerical results: ——, $a = 0.726$. —·—, $a = 0.914$. – – –, $a = 1.10$.

eventually attains comparable values with the smaller size for $Ca \geqslant 0.25$. The increase in U/V with increasing capillary number is simply due to larger drop deformation for larger capillary number and hence localization of the drop about the centreline of the tube where fluid velocities are greater. The decrease in ΔP^+ with increasing Ca is also strongly dependent on drop size (figure 12). Large drops ($a > 0.9$) show a rapid decrease in ΔP^+ for small capillary number (note the abscissa is a logarithmic scale) and a more gentle decrease with increasing capillary number. Smaller drops ($a = 0.726$) show a more modest decrease in the entire range of capillary number and show significant decrease in ΔP^+ only for $Ca > 0.5$. The decrease of ΔP^+ with increasing capillary number can be anticipated upon consideration of the discontinuity in normal stress at the interface stated in equation (6). The resistive forces of surface tension are strong when the capillary number is small and the difference in pressure across the interface is $O(\gamma/a_0)$. The major effect when $Ca \ll 1$ is to raise the level of pressure inside the nearly spherical drop as compared to the pressure exterior to the drop; the viscous stresses in the suspending fluid may yet yield significant dissipation as a result of the highly disturbed flow about an unyielding interface. Hence, even relatively inviscid drops can produce $\Delta P^+ > 0$ for very small capillary number as shown in figure 12 on the curve for $a = 0.914$ and $\lambda = 0.19$. This effect of capillary number is dependent on drop size, however. According to the analysis of Hyman & Skalak (1972*a*) for undeformed bubbles ($Ca \to 0$, $\lambda = 0$), $\Delta P^+ < 0$ for $a = 0.8$. Thus large capillary forces will result in positive additional pressure loss for relatively inviscid drops but only if $a > 0.8$.

4.4. *Effect of the viscosity ratio*

Some effects of the drop to suspending fluid viscosity ratio have already been discussed briefly in the foregoing; we give a more complete account of these effects in this section. The effect of drop viscosity on the general form of the flow field is

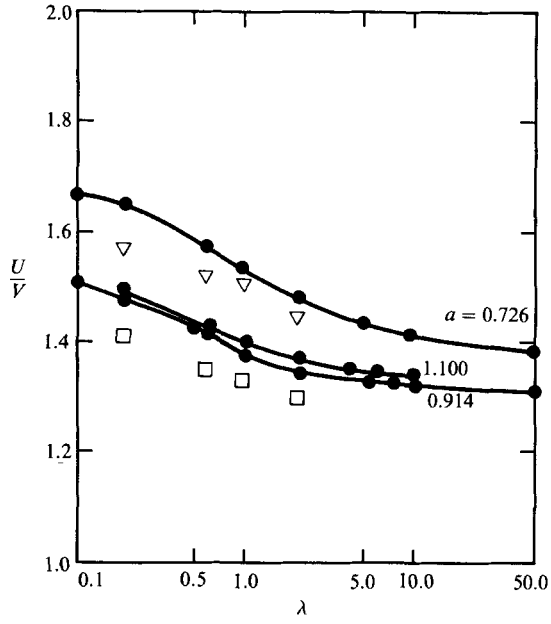

FIGURE 13. Effect of viscosity ratio on drop speed for $Ca = 0.10$; —●— present results; open symbols are the data of Ho & Leal (1975); ▽, $a = 0.726$; □, $a = 0.914$, 1.100.

illustrated in figures 3(*a*) and 3(*b*) which show that the viscous drop has a lower shear rate than does the less viscous drop. That is, the velocity distribution in the viscous drop is reminiscent of a rigid, neutrally buoyant axisymmetric body suspended in tube flow. In contrast, the less viscous drop displays a vigorous recirculation and two weak, though clearly visible, eddies in the nose and tail regions interior to the drop.

The shapes of the nose region of the profiles, shown in figure 4(*a*, *b*), are nearly unchanged with increasing drop size for the low-viscosity drop while the profiles variation is prominent for the more viscous drop, the profile curvature increasing with increasing drop size. At large capillary number, the profiles for small drops with large λ are wedge-shaped as shown in figure 9. It is also observed that the deformation increases with λ, all other parameters being equal. This effect of λ becomes clear in consideration of the normal stress jump condition at the interface, equation (6*b*), showing that both drop and suspending fluid viscosities are important. In particular, using continuity in a local normal–tangential (n–s) coordinate system, specialized for $v_n = u_n = 0$ on the interface,

$$\frac{\partial u_n}{\partial n} + \frac{1}{r}\frac{\partial (r u_s)}{\partial s} = 0,$$

and the no-slip condition, equation (6*a*), it follows that $\partial v_n/\partial n = \partial u_n/\partial n$, in which case the normal stress balance across the fluid interface can be written as

$$p_b - p + 2(1-\lambda)\frac{\partial u_n}{\partial n} = \frac{(\kappa - Bo\, z)}{Ca}.$$

In the case $\lambda = 1$, the normal viscous stresses cancel; in the general case, an increase in λ increases or decreases the capillary pressure jump, depending on the sign of $\partial u_n/\partial n$. Referring to figure 3, $\partial u_n/\partial n < 0$ about the leading stagnation ring and

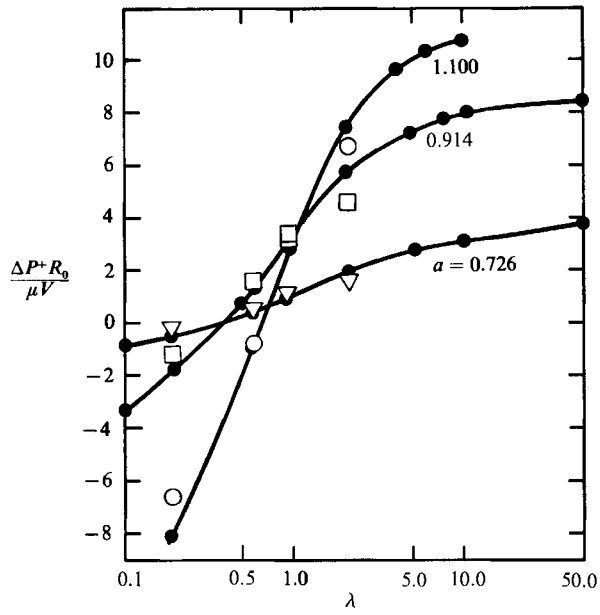

FIGURE 14. Effect of viscosity ratio on extra pressure decrease for $Ca = 0.10$; —●— present results; open symbols are the data of Ho & Leal (1975): ▽, $a = 0.726$; □, $a = 0.914$; ○, $a = 1.100$.

$\partial u_n/\partial n > 0$ about the trailing stagnation ring, indicating increased and decreased deformation in these respective regions for an increase in viscosity ratio. This interpretation of the effect of viscosity ratio on the normal stress condition elucidates the increase in deformation with increasing viscosity ratio, other parameters held fixed, and the wedge-shaped drops predicted at large viscosity ratios (figures 4, 9, and 10).

The effect of the viscosity ratio on the speed ratio and extra pressure loss is shown in figures 13 and 14 where U/V and ΔP^+ are plotted as functions of λ for $Ca = 0.1$ and $a = 0.726$, 0.914 and 1.10. The data reported by Ho & Leal for the same parameter values are also shown for comparison. As expected, $\partial(U/V)/\partial\lambda < 0$ for all λ but the rate of change is largest for $\lambda = O(1)$ and vanishes for $\lambda \to \infty$. The minimum of U/V with drop size discussed earlier is also apparent in figure 13.

Figure 14 shows that $\partial\Delta P^+/\partial\lambda > 0$ for all λ but the rate of change increases with drop size. However, ΔP^+ approaches an asymptotic value as $\lambda \to \infty$. It is also apparent from figure 14 that the sign of ΔP^+ depends on λ. In particular, the figure shows that suspensions of low-viscosity drops can be transported with less pressure gradient than if the tube contained only suspending fluid flowing at the same bulk volume flux. Lower viscosity drops reduce the shear stress between the drop and tube wall and hence reduce the dissipation and pressure loss. The value of λ where $\Delta P^+ = 0$ increases towards one as the drop size increases. The limiting value can be shown to be $\lambda = 1$ when $a \to \infty$ by considering the limiting case of two coflowing fluids in a tube, one of which flows in an annulus contiguous with the tube walls.

Figure 14 also shows that there exists a range in λ for which ΔP^+ has a maximum with respect to a. Thus, for the approximate range $0.4 \leqslant \lambda \leqslant 1$, ΔP^+ is greater for $a = 0.914$ than for the smaller and larger drop size. ΔP^+ is a monotonically decreasing or increasing function of a for $\lambda < 0.4$ and $\lambda > 1$. This effect is also evident in figure 8(*b*). The reason for this behaviour for certain viscosity ratio and drop size is the

competing effects of capillarity and of the simple exchange of lower or higher viscosity fluid in the volume occupied by the drop. The primary reason for $\Delta P^+ > 0$ when $\lambda < 1$ is the increased magnitude of the viscous stresses and hence enhanced viscous dissipation caused by the highly disturbed flow about an unyielding interface. For fixed Ca, this effect depends on the drop size. If the drop is small enough, the flow disturbance yields a negligible contribution to ΔP^+. When a is sufficiently large the reduction in volumetric dissipation by replacement of the drop volume with fluid of lower viscosity will more than compensate for the opposing effect of capillarity, resulting in $\Delta P^+ < 0$ if $\lambda < 1$. Finally, there is some intermediate drop size where the effect of the flow disturbance is sufficient to overcome the fluid replacement mechanism and yield a maximum value of ΔP^+, as illustrated in figures 8(*b*) and 14.

5. Conclusions

The flow of a viscous drop in a tube filled with a second immiscible viscous fluid has been analysed using a boundary integral equation method. The effects of the drop size, the ratio of viscous and surface-tension forces, and the viscosity ratio on the drop shape, drop speed, and the pressure gradient were examined.

In a reference frame fixed to the drop, there is a dividing streamtube separating the leak-back flow of suspending fluid from a bolus trapped ahead of and behind the drop. The dividing streamtube meets the interface to form a stagnation ring on the leading and trailing ends of the drop. A small eddy resides in the nose and tail regions interior to the drop.

The effects of the no-slip condition on the tube wall become important for $a \geqslant 0.7$. Smaller drops are insensitive to substantial variations in capillary number and viscosity ratio, and show significant deformation only when $Ca > 0.25$. The drop shape and speed are independent of drop size for $a \geqslant 1.10$. Further increases in drop volume result only in an increase in its length without change in shape of the leading or trailing menisci, or in the thickness of the film of suspending fluid surrounding the drop. The asymptotic film thickness increases with capillary number and viscosity ratio although the leak-back flux in the film decreases, relative to the bulk volume flux, with increasing viscosity ratio.

The drop deformation increases with capillary number and viscosity ratio, both of which act to diminish the normal stress difference on the fluid interface. The deformation has a stronger correlation to the capillary number, however. Drops of size $a = 0.726$ were found to develop negative curvature at the rear of the drop for $Ca \approx 0.75$.

The required additional pressure loss, owing to the presence of the drop, can be less or greater than that required for the suspending fluid alone, depending mainly on the viscosity ratio for moderate values of the capillary number. Drops with lower viscosity than the suspending fluid require less pressure gradient than would be necessary in their absence to maintain the same volume flux. However, strong interfacial forces ($Ca \ll 1$) can result in positive extra pressure decrease, even for $\lambda < 1$, if $a > 0.8$. The viscosity will ultimately determine the sign of ΔP^+ as $a \to \infty$.

Computed values of drop speed and extra pressure drop are in excellent agreement with the theoretical results of Hyman & Skalak (1972*a*) for small drop size. The comparison with the experimental data of Ho & Leal (1975) for undeformed radii comparable with the tube radius is also excellent for extra pressure decrease and satisfactory for drop speed.

This work was performed with financial support from Sandia National Laboratories under the Doctoral Studies Program.

REFERENCES

BRENNER, H. 1971 Pressure drop due to the motion of neutrally buoyant particles in duct flows. II. Spherical droplets and bubbles. *Indust. Engng Chem. Fund.* **10**, 537–543.

BRETHERTON, F. P. 1961 The motion of long bubbles in tubes. *J. Fluid Mech.* **10**, 166–188.

CHI, B. K. 1986 The motion of immiscible drops and the stability of annular flow. Ph.D. thesis, Cal. Inst. of Tech., Pasadena, California.

COX, B. G. 1962 On driving a viscous fluid out of a tube. *J. Fluid Mech.* **14**, 81–98.

DARCY, H. 1856 *Les Fontaines Publiques de la Ville de Dijon.* Paris: Victor Dalmont.

DAVIS, R. E. & ACRIVOS, A. 1966 The influence of surfactants on the creeping motion of bubbles. *Chem. Engng Sci.* **21**, 681–685.

DULLIEN, F. A. L. 1979 *Porous Media: Fluid Transport and Pore Structure.* Academic.

FAIRBROTHER, F. & STUBBS, A. 1935 Studies in electroendosmosis. Part VI. The bubble-tube methods of measurement. *J. Chem. Sci.* **1**, 527–529.

GOLDSMITH, H. L. & MASON, S. G. 1963 The flow of suspensions through tubes: II. Single large bubbles. *J. Colloid Sci.* **18**, 237–261.

HABERMAN, W. L. & SAYRE, R. M. 1958 Motion of rigid and fluid spheres in stationary and moving liquids inside cylindrical tubes. *David Taylor Model Basin Rep.* 1143. Washington D. C.

HAPPEL, J. & BRENNER, H. 1965 *Low Reynolds Number Hydrodynamics.* Prentice-Hall.

HESTRONI, G., HABER, S. & WACHOLDER, E. 1970 The flow field in and around a droplet moving axially within a tube. *J. Fluid Mech.* **41**, 689–705.

HO, B. P. & LEAL, L. G. 1975 The creeping motion of liquid drops through a circular tube of comparable diameter. *J. Fluid Mech.* **71**, 361–384.

HYMAN, W. A. & SKALAK, R. 1972*a* Viscous flow of a suspension of liquid drops in a cylindrical tube. *Appl. Sci. Res.* **26**, 27–52.

HYMAN, W. A. & SKALAK, R. 1972*b* Non-Newtonian behavior of a suspension of liquid drops in tube flow. *AIChE J.* **18**, 149–154.

LADYZHENSKAYA, O. A. 1969 *The Mathematical Theory of Viscous Incompressible Flow*, 2nd edn. Gordon and Breach.

MARTINEZ, M. J. 1987 Viscous flow of drops and bubbles in straight and constricted tubes. Ph.D. thesis, University of California, Berkeley.

MARTINEZ, M. J. & UDELL, K. S. 1989 Boundary integral analysis of the creeping flow of long bubbles in capillaries. *Trans. ASME* E: *J. Appl. Mech.* **56**, 211–217.

OLBRICHT, W. L. & LEAL, L. G. 1983 The creeping motion of immiscible drops through a converging/diverging tube. *J. Fluid Mech.* **134**, 329–355.

PAYATAKES, A. C. 1982 Dynamics of oil ganglia during immiscible displacement in water-wet porous media. *Ann. Rev. Fluid Mech.* **14**, 365–393.

PAYATAKES, A. C. & NEIRA, M. A. 1977 Model of the constricted unit cell type for isotropic granular porous media. *AIChE J.* **23**, 922–930.

PAYATAKES, A. C., TIEN, C. & TURIAN, R. M. 1973 A new model for granular porous media: Part II. Numerical solution of steady state Newtonian flow through periodically constricted tubes. *AIChE J.* **19**, 67–76.

PROTHERO, J. & BURTON, A. C. 1961 The physics of blood flow in capillaries. *J. Biophys.* **2**, 525–572.

RALLISON, J. M. & ACRIVOS, A. 1978 A numerical study of the deformation and burst of a viscous drop in an extensional flow. *J. Fluid Mech.* **89**, 191–200.

REINELT, D. A. & SAFFMAN, P. G. 1985 The penetration of a finger into a viscous fluid in a channel and tube. *SIAM J. Sci. Statist. Comput.* **6**, 542–561.

RIZZO, F. J. & SHIPPY, D. J. 1968 A formulation and solution procedure for the general non-homogeneous elastic inclusion problem. *Intl J. Solids Struct.* **4**, 1161–1179.

SCHEIDEGGER, A. E. 1974 *The Physics of Flow through Porous Media*, 3rd edn. University of Toronto Press.

SCHWARTZ, L. W., PRINCEN, H. M. & KISS, A. D. 1986 On the motion of bubbles in capillary tubes. *J. Fluid Mech.* **172**, 259–275.

SHEN, E. I. & UDELL, K. S. 1985 A finite element study of low Reynolds number two-phase flow in cylindrical tubes. *Trans. ASME* E: *J. Appl. Mech.* **52**, 253–256.

TAYLOR, G. I. 1961 Deposition of a viscous fluid on the wall of a tube. *J. Fluid Mech.* **10**, 161–165.

TELETZKE, G. F. 1983 Thin liquid films: molecular and hydrodynamic implications. Ph.D. thesis, University of Minnesota, Minneapolis, Minnesota.

WANG, H. & SKALAK, R. 1969 Viscous flow in a cylindrical tube containing a line of spherical particles. *J. Fluid Mech.* **38**, 75–96.

YOUNGREN, G. K. & ACRIVOS, A. 1975 Stokes flow past a particle of arbitrary shape: a numerical method of solution. *J. Fluid Mech.* **69**, 377–403.